Materials Today Advances 12 (2021) 100179

Contents lists available at ScienceDirect

Materials Today Advances

journal homepage: www.journals.elsevier.com/materials-today-advances/

Understanding how single-atom site density drives the performance and durability of PGM-free Fe—N—C cathodes in anion exchange membrane fuel cells

Horie Adabi [a, 1], Pietro Giovanni Santori [b, 1], Abolfazl Shakouri [a], Xiong Peng [a], Karam Yassin [d], Igal G. Rasin [d], Simon Brandon [d, e], Dario R. Dekel [d, e], Noor Ul Hassan [a], Moulay-Tahar Sougrati [b], Andrea Zitolo [f], John R. Varcoe [c], John R. Regalbuto [a], Frédéric Jaouen [b, **], William E. Mustain [a, *]

[a] Department of Chemical Engineering, University of South Carolina, Columba, SC USA
[b] ICGM, Univ. Montpellier, CNRS, ENSCM, Montpellier, France
[c] Department of Chemistry, University of Surrey, Guildford, UK
[d] The Wolfson Department of Chemical Engineering, Technion – Israel Institute of Technology, Haifa 3200003, Israel
[e] The Nancy & Stephen Grand Technion Energy Program (GTEP), Technion – Israel Institute of Technology, Haifa 3200003, Israel
[f] Synchrotron SOLEIL, L'orme des Merisiers, BP 48 Saint Aubin, 91192 Gif-sur-Yvette, France

ARTICLE INFO

Article history:
Received 26 July 2021
Received in revised form
1 October 2021
Accepted 4 October 2021
Available online xxx

Keywords:
PGM-free
AEM
Fuel cell
Oxygen reduction
High performance
Fe—N—C
Single-atom

ABSTRACT

One of the most important needs for the future of low-cost fuel cells is the development of highly active platinum group metal (PGM)-free catalysts. For the oxygen reduction reaction, Fe—N—C materials have been widely studied in both acid and alkaline media. However, reported catalysts in the literature show quite different intrinsic activity and in-cell performance, despite similar synthesis routes and precursors. Here, two types of Fe—N—C are prepared from the same precursor and procedure – the main difference is how the precursor was handled prior to use. It is shown that in one case Fe overwhelmingly existed as highly active single-metal atoms in FeN_4 coordination (preferred), while in the other case large Fe particles coexisting with few single metal atoms were obtained. As a result, there were drastic differences in the catalyst structure, activity, and especially in their performance in an operating anion exchange membrane fuel cell (AEMFC). Additionally, it is shown that catalyst layers created from single-atom-dominated Fe—N—C can have excellent performance and durability in an AEMFC using H_2/O_2 reacting gases, achieving a peak power density of 1.8 W cm^{-2} – comparable to similar AEMFCs with a Pt/C cathode – and being able to operate stably for more than 100 h. Finally, the Fe—N—C cathode was paired with a low-loading PtRu/C anode electrode to create AEMFCs (on H_2/O_2) with a total PGM loading of only 0.135 mg cm^{-2} (0.090 $mg_{Pt}\,cm^{-2}$) that was able to achieve a very high specific power of 8.4 W mg_{PGM}^{-1} (12.6 W mg_{Pt}^{-1}).
© 2021 The Author(s). Published by Elsevier Ltd. This is an open access article under the CC BY license (http://creativecommons.org/licenses/by/4.0/).

1. Introduction

Polymer electrolyte membrane fuel cells are a potentially ultralow CO_2-emission energy source if fueled with renewably-generated H_2. They have been widely touted for future stationary, transportation, and portable power applications [1]. Among such fuel cells, proton exchange membrane fuel cells (PEMFCs) have demonstrated high power density and durability. However, their reliance on Pt to catalyze the reaction in both electrodes, and in particular their relatively high loadings to enable the oxygen reduction reaction (ORR), leads to high cost [2,3]. Pt catalysts account for *ca.* 41% of the cost of a PEMFC stack, even for low production volumes [4]. Therefore, there is a strong incentive to replace Pt-based catalysts at the cathode of fuel cells with platinum group metal (PGM)-free catalysts.

Because of their high-pH environment, anion exchange

* Corresponding author.
** Corresponding author.
E-mail addresses: frederic.jaouen@montpellier.fr (F. Jaouen), mustainw@mailbox.sc.edu (W.E. Mustain).
[1] indicates equal contribution.

https://doi.org/10.1016/j.mtadv.2021.100179
2590-0498/© 2021 The Author(s). Published by Elsevier Ltd. This is an open access article under the CC BY license (http://creativecommons.org/licenses/by/4.0/).

membrane fuel cells (AEMFCs) provide a more benign operating environment than PEMFCs [1,3], allowing for a broader range of materials to be used for the catalysts, membranes and bipolar plates [5]. The possibility to deploy lower-cost materials throughout the cell has led many to tout AEMFCs as a possibly lower-cost fuel cell system than PEMFCs [6,7]. AEMFCs have also become more attractive in recent years as their performance and durability have significantly improved. For example, Huang et al. have achieved a peak power density of 3.5 W cm^{-2} for an AEMFC with H_2/O_2 gas feeds and electrodes based on PGMs [8], while Ul-Hassan et al. reported a high-performing cell with a decay rate of only *ca* 15 μV h^{-1} over more than 2000 h of operation [9]. However, these recent accomplishments have been obtained with high PGM loadings at both the anode and cathode electrodes.

To achieve the cost reductions promised by AEMFCs, active and robust PGM-free electrodes must be developed. Recently, the U.S. Department of Energy (DOE) has set the objective of reaching PGM-free AEMFCs by 2030 [6], with intermediate targets for the PGM loading of 0.2 mg cm^{-2} for 2021–2023 and ⩽ 0.125 mg cm^{-2} by 2024 [6]. One possible pathway to achieve these interim targets is to eliminate PGM from one electrode while strongly reducing the PGM loading at the other electrode. Since even the most active PGM-free catalysts investigated to date for the hydrogen oxidation reaction have resulted in much lower AEMFC performance than PGM-based anodes [1], the most promising pathway in the near future is to develop high-performance PGM-free cathodes and combine them with low-PGM anodes.

During the last decade, several classes of materials have been investigated as PGM-free catalysts for the ORR in alkaline media [10–17] and AEMFCs [18–22] such as silver, chalcogenides, spinel and perovskite structures, M-N-C (M = Fe, Co) catalysts and metal-free doped carbons. Among these, Fe–N–C catalysts with Fe being present only or mainly as atomically-dispersed FeN_4 moieties have shown the highest ORR mass-activity in rotating disk electrode (RDE) tests [21,23,24]. Several recent studies have also claimed a positive synergy between Fe particles (metallic Fe, iron carbide, iron nitride, hematite) and FeN_4 moieties [25–28]. Such a synergy might help overcome issues related with the low site density (SD) of FeN_4 moieties in Fe–N–C materials [29]. Moreover, while Fe–N–C catalysts have low *operando* stability in acidic media and in PEMFCs [30–33], due to several degradation mechanisms [34–37], this is less of a concern in alkaline media. One example is free radical attack from peroxide radicals. During the ORR, small amounts of hydrogen peroxide are generated [38]. In acid media, H_2O_2 is quite stable and reacts at the Fe sites to form radicals that can attack the membrane and ionomer. At higher pH, like in AEMFCs, hydrogen peroxide has a much higher self-decomposition rate. Thus, two recent studies have shown negligible deactivation for Fe–N–C catalysts after exposure to hydrogen peroxide in pH ⩾10 electrolytes, while strong deactivation was observed after exposure to hydrogen peroxide in acidic environments [39,40]. Hence, it can be expected that Fe–N–C catalysts will be significantly more durable in operating AEMFCs, though questions about the stability of the carbon matrix itself in alkaline medium remain [41–43].

However, not much is known about the *operando* stability of Fe–N–C catalysts in AEMFCs. The two most likely reasons for this are: i) a history of significantly lower initial power performance of AEMFCs with Fe–N–C cathodes compared to those incorporating state-of-the-art Pt-based cathodes [20,44,45]; and ii) poor water management, which until recently also prevented running AEMFCs stably with PGM-based electrodes as well. A promising fact, however, is that several Fe–N–C cathodes have closely approached or even surpassed the performance of state-of-the-art Pt-based cathodes at 0.9 V cell voltage, *i.e.* under the kinetically-controlled regime. Altogether, this strongly suggests that mass-transport issues are exacerbated in Fe–N–C cathodes compared to Pt/C cathodes. There are two main explanations for this: either the FeN_4 sites are intrinsically less accessible (*e.g.*, because of their location in micropores), or the lower accessibility is an indirect effect of the low site density (SD) of FeN_4 moieties. Except for a recent work [46], the highest reported SD of FeN_4 sites for an Fe–N–C material had been hitherto ~$6x10^{19}$ sites/g [29], about one order of magnitude lower than the number of Pt sites in a typical 40–50 wt% Pt/C catalyst (~$8x10^{20}$ sites/g [47]). This means that for a similar loading of carbon (*i.e.* for a similar thickness of the catalyst layer), the number of FeN_4 sites per geometric area is only 1/10th of the Pt sites. Hence, in an AEMFC operating at a given current density, the ORR turnover frequency at an FeN_4 site is *ca* ten-times higher than that at a Pt site. This could lead to severe issues of localized mass transport near FeN_4 sites and that are not experienced by Pt sites. It is therefore critical to understand how the SD value of Fe–N–C catalysts drives the AEMFC performance, especially at high current densities. Similarly, it is important to establish the durability of Fe–N–C cathodes in operating AEMFCs and an understanding of their performance loss over time.

In this work, two Fe–N–C catalysts were prepared with similar pore structures, macroscopic morphology and total Fe content. One catalyst was comprised of almost entirely single-atom Fe–N_4 moieties while the other contained a mix of FeN_4 moieties and Fe nanoparticles. This allowed for the investigation of both the effect of SD and a possible synergy between FeN_4 and Fe nanoparticles on their ORR activity, selectivity and performance. The structure, porosity and morphology of the two catalysts were characterized *ex situ* using a suite of tools that give access to macroscopic features, but also atomic-level insights into the Fe dispersion and coordination. The activity and selectivity of both catalysts were first investigated with a rotating ring disk electrode (RRDE) and their activity and power performance were then investigated in AEMFCs. The best-performing Fe–N–C catalyst was paired with an optimized low-PGM loading anode to achieve a high performance, low-PGM membrane electrode assembly (MEA). Finally, an AEMFC with best-performing Fe–N–C cathode was subjected to a 105 h durability test and the degradation behavior was investigated by electrochemical techniques, *post mortem* ^{57}Fe Mössbauer spectroscopy, and applying a comprehensive physico-chemical model of the entire MEA.

2. Experimental

2.1. Synthesis of the Fe–N–C catalysts

Two Fe–N–C materials with natural iron were prepared and investigated in this work, the synthesis differing only in the use of either anhydrous ferrous acetate or ferric acetate hydrate as the iron precursor, denoted here as $Fe_{0.5}$-dry and $Fe_{0.5}$-hydrate, respectively. A third Fe–N–C material was prepared as $Fe_{0.5}$-dry, but with isotopic ^{57}Fe(II) anhydrous acetate ($^{57}Fe_{0.5}$-dry), which allowed for *post mortem* Mössbauer spectroscopy to be performed. A schematic for the overall synthesis procedure is shown in Supplementary Fig. 1. The catalysts were prepared relying on the use of a sacrificial metal-organic framework, namely ZIF-8, and phenanthroline as the sources of carbon. Previous work from our team showed that wet impregnation of Fe(II) acetate, phenanthroline and ZIF-8 in aqueous solution before drying the mixture and pyrolyzing it resulted in a large amount of Fe being present as metallic and carbide particles (47%), the remainder being FeN_4 moieties (53%) [48]. In contrast, the same synthesis but bypassing the wet impregnation step resulted in Fe atoms being present mainly as FeN_4 sites (94% of Fe, comparison made at 1 wt% Fe

content before pyrolysis) [48,49]. Here, we resorted to both anhydrous Fe(II) acetate and hydrate Fe(III) acetate as iron sources to investigate the effect of oxidation state and amount of water in iron acetate precursors on the Fe speciation and properties of Fe−N−C catalysts in alkaline media. For both catalysts, 800 mg of commercial ZIF-8 (Basolite® Z1200), 200 mg of 1,10-phenantroline (≥99% purity) and the mass of iron acetate (≥99.99% purity) necessary to reach 0.5 wt% Fe in the catalyst precursor were poured in a zirconia-lined jar together with 100 zirconia beads (5 mm diameter). The anhydrous Fe(II) acetate was purchased (Sigma Aldrich) and stored in a glove box, while the hydrate Fe(III) acetate was obtained by aging anhydrous Fe(II) acetate in ambient conditions. The spontaneous transformation from Fe(II) to Fe(III) acetate was experimentally verified (see Results). ^{57}Fe(II) anhydrous acetate was purchased from Porphyrin Laboratories GmbH and stored in a glove box. The catalyst precursors were mixed without any addition of solvents using planetary ball milling at 400 rpm for four consecutive cycles, each cycle composed of 25 min milling followed by a 5 min pause. The powder was then collected from the jar, transferred in a quartz boat and inserted into a quartz tube. For the first pyrolysis, the oven was pre-equilibrated at 1050 °C for 2 h while a continuous flow of Ar passed through the tube, with the quartz boat and catalyst precursor inside the tube, but outside the heating zone. After 2 h, the quartz boat was pushed into the heating zone in three steps of 30 s ("flash pyrolysis") with the help of an outer magnet and a quartz rod with a magnet attached at one end, located inside the tube. The catalyst precursor was then pyrolyzed in Ar at 1050 °C for 1 h, after which the oven was opened and the tube removed and let to cool down for 20 min under Ar flow. A second pyrolysis step was then performed, following the above-mentioned procedure, but under pure NH_3 flow, an oven temperature of 950 °C and a pyrolysis duration of 5 min. The final products were collected from the quartz boat and used as-is. Since i) the Fe content before pyrolysis was the same for both catalysts, ii) the mass loss during pyrolysis (C, N and O volatile species, while all Fe remains, as shown in our previous works, [48]) is comparable for both syntheses, and iii) no acid-leaching or other post-treatment was applied, it can be deduced that the total Fe contents in the final catalysts are similar.

2.2. Structural characterization

Powder XRD patterns of the Fe acetate precursors and the Fe−N−C catalysts were recorded using either a Rigaku Miniflex-II equipped with a high sensitivity D/teX Ultra silicon strip detector or a PANanalytical X'Pert Pro powder X-ray diffractometer. Patterns were collected over a range of 10°−90° using Cu-Kα radiation (k = 1.5406 Å) at 30 mA and 15 kV. A ZEISS Gemini 500, 0.02−30 kV Ultra plus Thermal FESEM equipped with an Inlens secondary electron detector and EDS (energy dispersive x-ray spectroscopy) detector was used to evaluate the catalyst pore structure and elemental distribution. The SEM images were collected at an electron beam energy of 5 kV, and the EDS mapping was carried out at an electron beam energy of 20 kV. To complement the pore analysis, a Micromeritics ASAP 2020 Plus was utilized to perform N_2 adsorption experiments, allowing the pore size distribution and BET surface area to be calculated for both catalysts. NLDFT analysis with SAIEUS software was employed to determine the pore size distribution. ^{57}Fe Mössbauer spectroscopy was acquired on the Fe acetates, Fe−N−C catalysts and Fe−N−C cathode, at room temperature or at 5 K using a ^{57}Co:Rh source, and applying a triangular velocity waveform using NaI scintillation detector for γ-rays. The velocity calibration was performed with an α-Fe foil.

A Hitachi HT7800 RuliTEM equipped with a standard lens for high contrast and resolution of 0.204 nm (Off-axis, 100 kV) was used to capture bright-field images of the Fe−N−C catalysts. For that purpose, the catalysts were deposited onto a holly carbon-coated transmission electron microscopy (TEM) copper grid and images were captured at an electron energy of 100 kV. For high-resolution scanning transmission electron microscopy (STEM) imaging, a JEOL 2100F 200 kV, equipped with a CEOS Cs corrector on the illumination system, was used for Z-contrast imaging. High angle annular dark-field (HAADF) STEM images were captured with a Fischione Model 3000 HAADF detector with a camera length such that the detector spanned 50−250 mrad. The scanning acquisition was synchronized to 60 Hz AC electrical power to minimize 60Hz noise in the images, and a pixel dwell time of 15.7μs was chosen. The catalyst sample was suspended in isopropanol and dispersed using ultrasonic vibration for 1 min. A droplet of the suspension was then placed on a holly carbon-coated (mesh 200, SPI Inc.) TEM copper grid with a platinum ring. A filter paper underneath the TEM grid absorbed the liquid that passed through the carbon-coated TEM grid, and the particles were deposited onto the carbon mesh. The sample was cleaned using an electron beam shower under vacuum for 15 min to clean any chemical residue from the surface.

Fe K-edge X-ray absorption spectra of anhydrous and aged Fe(II) acetate, and of 0.1 M Fe(III) water solution were recorded at room temperature in transmission mode at the SAMBA beamline of Synchrotron SOLEIL, using a sagittaly focusing Si(220) monochromator. Iron(II) acetate samples were pelletized as disks of 10 mm using boron nitride as binder, while the Fe(III) water solution was prepared by dissolving $FeCl_3$ in deionized water at pH 4.

2.3. Rotating (ring) disk electrode measurements

The ORR activity and selectivity of the Fe−N−C materials were measured with a RRDE setup (Pine Instruments) in aqueous 0.1 M KOH. The reference electrode was a reversible hydrogen electrode (RHE) made from a Pt-wire immersed in a H_2-saturated electrolyte separated from the main compartment by a fritted glass. The counter electrode was a graphite rod. There were two working electrodes that were used: a RDE with a 5.0 mm glassy carbon disk and a RRDE with a 5.6 mm diameter glassy carbon disk and Pt ring. The Pt ring was used to quantify the amount of produced peroxide. The catalyst was introduced onto the disk electrodes by first preparing an ink containing 54 μL of Nafion® (5% perfluorinated resin solution), 744 μL of ethanol and 92 μL of ultrapure water and 5 mg of Fe−N−C. The ink was homogenized by sonication for 1 h. Then, an aliquot of the ink was deposited on the electrode, 8.8 μL for the RRDE tip and 7 μL for the RDE tip, leading to a catalyst loading of 0.2 mg cm^{-2}. The inks were dried in air at room temperature. To measure the ORR activity and selectivity, the solution was saturated with O_2 and the potential scanned in the range 0.0−1.0 V *vs*. RHE at 5 mV s^{-1}, while a constant potential of 1.2 V *vs*. RHE was applied to the Pt ring. To measure the electrochemical capacitance in N_2 saturated KOH, a scan rate of 10 mV s^{-1} was applied.

2.4. Preparation of anode and cathode gas diffusion electrodes (GDEs)

Gas diffusion electrodes (GDEs) were fabricated using a previously developed method [50,51]. To create the cathodes and "standard" anodes (with high PGM loading), inks were prepared from a combination of the ionomers, a solvent mixture of deionized water (DI, 18.2 MΩ, Millipore) H_2O and isopropyl alcohol, non-catalyst Vulcan XC-72R carbon, and the electrocatalyst [50,51]. For the cathodes, the catalyst was either the synthesized Fe−N−C powder or a commercial Pt/C (Alfa Aesar HiSPEC 4000, Pt nominally 40 wt%, supported on Vulcan XC-72R carbon). The anode catalyst

was always PtRu/C (Alfa Aesar HiSPEC 10000, Pt nominally 40%wt., and Ru, nominally 20%wt., supported on Vulcan XC-72R carbon). The anion exchange ionomer (AEI) was an ETFE-BTMA powder with an IEC of 1.24 ± 0.06-meq g^{-1} [52], water uptake of 155.4 ± 1.8%, and an average particle size of 24.5 ± 9.8 μm. To begin the ink making process, which is described in detail in a previous publication [9], 56.25 mg of the AEI was ground in a clean mortar and pestled for 10 min to reduce the size and number of large agglomerates of ionomer particles. Next, 150 mg of catalyst powder, 75 mg of non-catalyzed Vulcan XC-72R and 1.0 mL of Millipore deionized water (DI, 18.2 MΩ cm) were added into the mortar and ground for an additional 10 min, until a visually and texturally homogeneous slurry formed. Then, 1.5 mL of isopropanol was added into the mortar, followed by another 5 min of grinding, followed by a final additional volume of 5 mL of isopropanol. Next, the ink was transferred to a PTFE-lined vial along with 24.46 mg of PTFE dispersion (Ultraflon MP-25, Fuel Cell Store) where it was sonicated for 1 h in an ice bath. The final inks were sprayed onto a Toray 60 gas diffusion layer (GDL) with 5 wt% PTFE wetproofing using an air-assisted spray gun (Iwata) to fabricate the GDEs. The targeted loadings were 1.0–1.2 $mg_{Fe\text{-}N\text{-}C}$ cm^{-2}, 0.4–0.6 mg_{Pt} cm^{-2} and 0.5–0.7 mg_{PtRu} cm^{-2} for the non-PGM cathodes, PGM cathodes and high PGM loading anodes, respectively.

In addition to the "standard" anodes, four types of low-PGM loading PtRu/C anodes were made, denoted as LPGM-A1, LPGM-A2, LPGM-A3 and LPGM-A4. LPGM-A2 was made using the procedure described above for the standard anode, except that the amount of material deposited was reduced to reach a PGM loading of ca. 0.2 mg_{PGM} cm^{-2}. LPGM-A1 was made as LPGM-A2, except that no PTFE was added in the ink preparation. For the LPGM-A3 GDEs, a lower content of PtRu on C was used (10 wt% PtRu/C, Fuel Cell Store), while the ionomer:carbon ratio was the same as in the standard anode. The LPGM-A4 electrode was made from two layers. First a microporous layer (MPL) was deposited onto the GDL, followed by the deposition of the PtRu/C catalytic layer. The ink for MPL was prepared by sonicating the AEI with Vulcan XC-72R (AEI:C ratio of 0.417:1 by wt.), PTFE dispersion (such that the final solid fraction of PTFE was 8 wt%) and isopropyl alcohol in a PTFE-lined vial for 1 h. Next, the catalytic layer was sprayed on top of the MPL. The composition of the catalytic layer was the same as the LPGM-A2 electrode.

2.5. Fuel cell assembly and testing

The anion exchange membranes (AEMs) used in this study were radiation-grafted high-density polyethylene (HDPE) film (25 μm, IEC = 2.8 ± 0.1 mmol g^{-1}) with covalently-bound benzyltrimethylammonium (BTMA) cationic head-groups [71]. The AEM, anode and cathode GDEs were hydrated in DI water for 20 min and then soaked three times for 20 min each time (60 min total) in aqueous 1.0 M KOH solution in order to remove impurities and to ion-exchange all quaternary ammonium groups into the hydroxide form. After soaking, excess KOH was removed from the electrodes and membrane. Next, the AEM, anode and cathode were assembled, without prior hot pressing, in a 5 cm^2 active area Scribner fuel cell hardware with single-channel serpentine flow fields. The AEMFCs were controlled by a Scribner 850e fuel cell test station. After a break-in procedure, the relative humidity (RH) of both the cathode and anode were adjusted to optimize the cell performance at the operating temperature (either 65 or 80 °C). The gases used in this study were ultra-high purity (UHP) H_2, UHP O_2 and simulated CO_2-free air (a mixture of UHP N_2 and O_2) from Airgas.

3. Results and discussion

3.1. Structural characterization of the Fe acetate precursors

Supplementary Fig. 2a shows the XRD patterns of the as-received anhydrous Fe(II) acetate salt (blue curve) and of the same salt but after aging in ambient conditions (red curve). As shown by Cheng et al. and Weber et al., anhydrous Fe(II) acetate salt has a long-range crystalline structure, which corresponds to a 2D mesoporous metal-organic framework involving Fe(II) cations and acetate ligands [54,55]. In contrast, the aged Fe(II) acetate salt only shows broad peaks, indicating an amorphous structure without long-range order. This XRD pattern is in line with that expected for Fe(III) acetate hydrate [56].

The oxidation and spin states of Fe in the two salts were then investigated with ^{57}Fe Mössbauer spectroscopy. Supplementary Fig. 2b shows the experimental spectrum of the fresh anhydrous Fe(II) acetate salt and its fitting with two quadrupole doublets. The doublets with a high isomer shift (IS) of 1.1 mm s^{-1} are easily assigned to Fe(II) in high spin state. This IS and quadrupole splitting (QS) value of *ca* 2.1 mm s^{-1} match those reported earlier for Fe(II) in the anhydrous Fe(II) acetate salt crystal [55]. Cheng et al. also fitted the room-temperature Mössbauer spectrum with two doublets with IS/QS values similar to those found here for the doublet represented in blue. These two doublets were assigned to an octahedral Fe(II)–O_6 coordination in an extended crystal of Fe(II) acetate, with two slightly different coordination environments. The detailed crystal structure of the Fe(II) acetate MOF was resolved in 2011, wherein all acetate ligands bridge two or more Fe(II) cations, and the unit cell comprises three Fe(II) cations [54]. The spectrum of the fresh anhydrous Fe(II) acetate also contains a minor amount of a second doublet (representing 20% of the total absorption signal), with low IS of 0.21 mm s^{-1} and QS of 0.9 mm s^{-1}. This doublet (represented in red) is assigned to Fe(III) and is an impurity present in the commercial Fe(II) acetate product during synthesis, or is due to initiated degradation of the Fe(II) acetate salt MOF upon contact with ambient air.

The ^{57}Fe Mössbauer spectrum of the aged Fe(II) acetate salt could be fitted with only one doublet, with IS and QS of 0.43 and 0.76 mm^{-1}, respectively (Supplementary Fig. 2c). Those values are in line with those reported for as-prepared Fe(III) acetate and also for anhydrous Fe(II) acetate after aging in ambient air [56,57]. Ferric acetate is known to form a trinuclear iron cation with formula $[Fe_3O(CH_3COO)_6(H_2O)_3]^+$ [56,58] in which the three Fe atoms are coordinatively equivalent, and bound by six oxygen ligands. Ferric acetate does not typically have long-range ordering, explaining its amorphous XRD pattern. From these characterizations, one can conclude that the commercial anhydrous Fe(II) acetate used for the present work is indeed mainly the expected Fe(II) acetate MOF but contains also *ca* 20% Fe as ferric acetate, while the aged acetate contains only Fe(III), and in the form of the trinuclear iron cation. While the fact that Fe(II) acetate can degrade in ambient air is well known by chemists, the detailed phenomena are less known. Here, it is shown that there is not only a change in the Fe oxidation state but also a structural change (from a crystalline MOF to a trinuclear Fe cation) and the inclusion of at least three water molecules in the trinuclear ferric acetate cation. It is possible that even more water is present, though with weaker bonding. The two salts were also characterized by X-ray absorption near edge spectroscopy (XANES) (Supplementary Fig. 2d). The XANES spectra confirm the lower oxidation state of Fe in as-received anhydrous Fe(II) acetate than in the aged Fe acetate, as can be seen from the different positions of the absorbing edge (Supplementary Fig. 2d). In addition, the XANES spectrum for the aged Fe acetate is very similar to the spectrum acquired for Fe(III) in aqueous solution. The results therefore

support the presence of a significant amount of water in the aged Fe(III) acetate, which we refer to henceforth as Fe(III) acetate hydrate.

3.2. Structural and chemical characterization of the Fe–N–C catalysts

Fig. 1a–b shows the XRD patterns of the two Fe–N–C catalysts. $Fe_{0.5}$-dry shows only weak diffraction peaks at 35.1°, 43.1°, 47.1°, 50.6° and *ca* 60.0°. The peaks at 35.1 and 60.0° match with the two most intense peaks expected for the iron nitride crystalline structure FeN (Fig. 1c) while the peak at 43.1° matches with the main peak expected of some Fe-rich nitrides, and especially for $Fe_3N_{1.39}$ (Fig. 1c). The $Fe_3N_{1.39}$ phase was also observed by XRD after a pyrolysis in ammonia of an Fe-doped ZIF-8 precursor [59]. The low intensity peaks at 47.1° and 50.6° match with some of the secondary diffraction peaks expected for Fe_3C (Fig. 1c). However, the reference material Fe_3C shows a series of intense diffraction peaks at 43.7–45.9° that are not observed in the XRD diffraction pattern of $Fe_{0.5}$-dry. Possibly, a minor fraction of Fe atoms formed Fe_3C during the first pyrolysis in Ar, and Fe_3C was partially nitrided during the subsequent short pyrolysis in NH_3, leading to metastable iron-carbon-nitride phases with ill-defined structure in $Fe_{0.5}$-dry. Also, it can be concluded from XRD that $Fe_{0.5}$-dry contains no or a very small amount of α-Fe phase, since the main diffraction peak for α-Fe at 44.6° is not observed (Fig. 1c). Overall, $Fe_{0.5}$-dry shows only weak diffraction peaks related to iron-containing phases, suggesting that most Fe atoms are present as atomically-dispersed FeN_x moieties. In contrast, $Fe_{0.5}$-hydrate shows a sharp diffraction peak at *ca* 42.8° and three other peaks at 37.5°, 40.7° and 56.8°, all matching the position and relative intensity of the XRD pattern of the iron nitride phase $Fe_3N_{1.39}$ (Fig. 1c). A weak and broad peak is also visible at 34.8–35.4°, possibly related to the main diffraction line for the iron nitride FeN phase.

Since Fe–N–C materials previously prepared by our team with the same synthesis and using anhydrous Fe(II) acetate resulted in no diffraction peaks related to iron [2], we surmise that the aging of Fe acetate and its partial (20% Fe(III) in the fresh commercial ferrous acetate) or complete transformation into Fe(III) acetate hydrate after aging is the key reason for the observation of small and large amounts of Fe particles for $Fe_{0.5}$-dry and $Fe_{0.5}$-hydrate, respectively, in the present work. The presence of water in the aged salt likely leads to hygroscopic effects leading to inhomogeneous dispersion with ZIF-8/phenanthroline and clustering of the Fe salt before pyrolysis. During the first pyrolysis in Ar, such clusters would likely form metallic iron or iron carbide particles, which can be converted to iron nitride particles during the second pyrolysis in pure NH_3. The generally lower intensity of Fe-related diffraction peaks in $Fe_{0.5}$-dry compared to $Fe_{0.5}$-hydrate suggests that the former contains a higher relative fraction of Fe as atomically dispersed FeN_4 sites. This hypothesis is further supported by ^{57}Fe Mössbauer spectroscopy, discussed later in this work.

To probe the morphology of the Fe–N–C catalysts, dispersion of Fe, as well as the size and distribution of any Fe-rich particles, high-resolution microscopy was used. First, SEM images with EDS mapping were collected, and representative images are shown in Supplementary Fig. 3. $Fe_{0.5}$-dry had a more open macroscopic porous structure than $Fe_{0.5}$-hydrate, as can be seen in high-resolution SEM images (Supplementary Fig. 3j compared to Supplementary Fig. 3d). Elemental mapping at this scale does not, however, identify the presence of Fe clusters or particles; the EDS mappings show only a uniform signal for C, N, O and Fe for both catalysts (Supplementary Fig. 3b,c,e,f and S3h,i,k,l). A higher resolution is needed to distinguish Fe particles from FeN_4 sites, which was obtained with STEM.

Z-contrast STEM imaging showed that $Fe_{0.5}$-hydrate contained many Fe particles of different sizes up to 80 nm, and the particles were spread throughout the catalyst (Fig. 2a), in line with XRD characterization. Many Fe particles *ca* 1 nm in size (confirmed as metallic Fe using image processing software to determine the

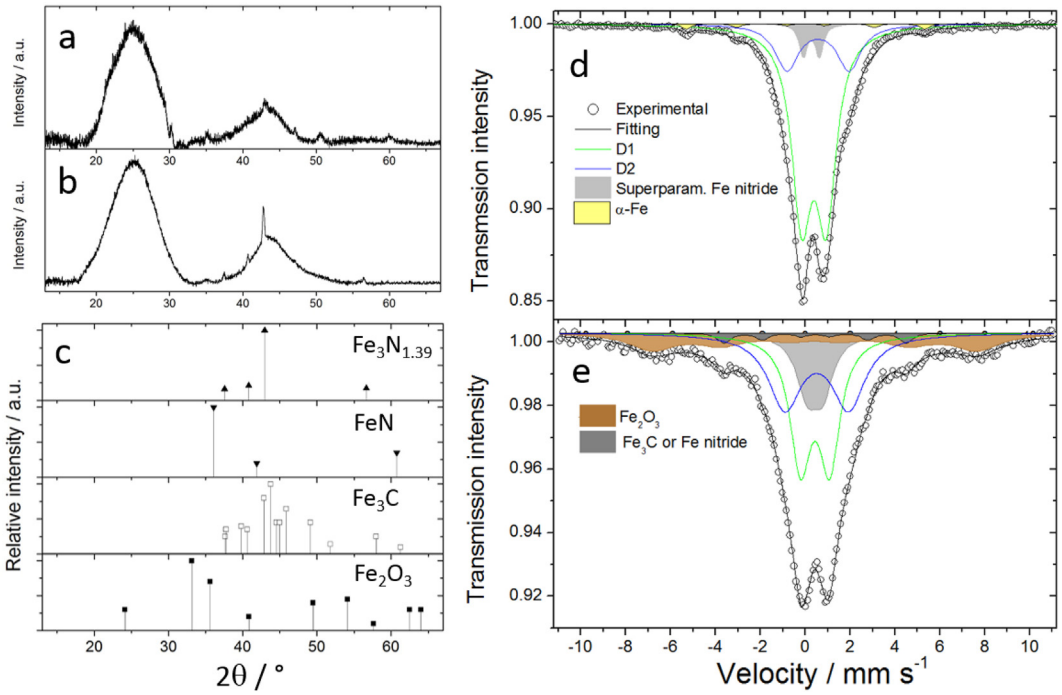


Fig. 1. Structural characterization of $Fe_{0.5}$-dry and $Fe_{0.5}$-hydrate. XRD patterns for a) $Fe_{0.5}$-dry and b) $Fe_{0.5}$-hydrate. c) XRD patterns for reference compounds. ^{57}Fe Mössbauer spectra for d) $Fe_{0.5}$-dry and e) $Fe_{0.5}$-hydrate. For c), the most intense diffraction peaks are represented for $Fe_3N_{1.39}$ (JCPDS file 04-023-4686, FeN (00-050-1087), Fe_3C (00-034-0001) and Fe_2O_3 (00-033-0664). Mössbauer spectra were acquired at 5 K.

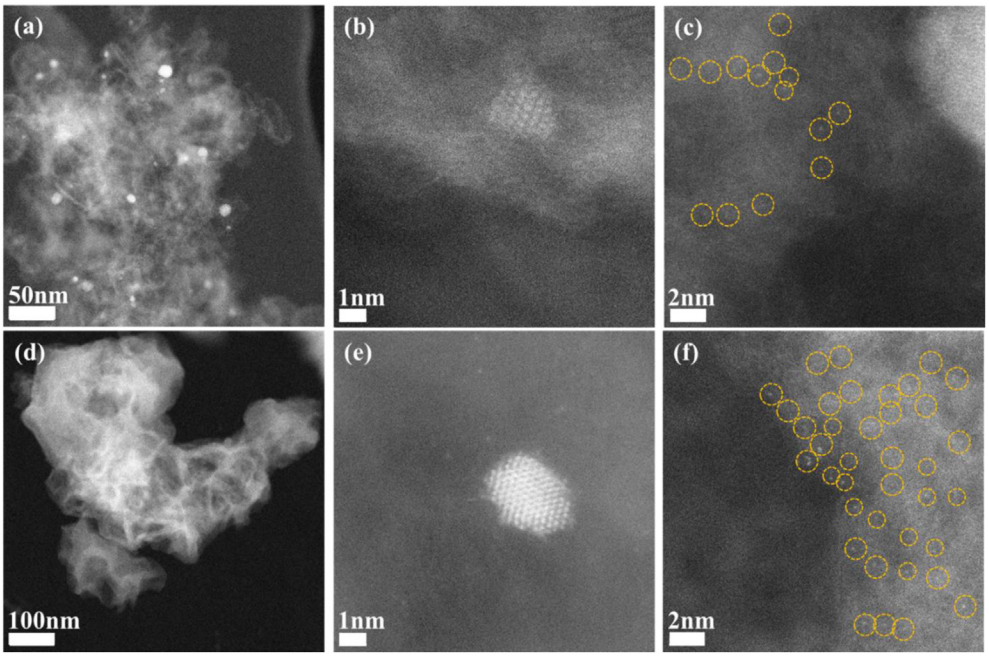


Fig. 2. ADF-STEM images of $Fe_{0.5}$-hydrate and $Fe_{0.5}$-dry. Images of $Fe_{0.5}$-hydrate showing (a) large Fe particles with different sizes, (b) small Fe particle with no single Fe atom around the particle, (c) some single Fe atoms away from sintered particles, and images of $Fe_{0.5}$-dry (d) showing no large Fe particles, (e) nanoparticle with several single Fe atoms nearby, (f) single Fe atoms dispersed on the carbon support.

lattice spacing as shown in Supplementary Fig. 4) also coexisted with these relatively large particles (Fig. 2b). The presence of these Fe nanoparticles lowers the number of single-atom FeN_4 active centers in the catalyst. In fact, no single Fe atoms were observed in the vicinity of Fe particles (Fig. 2b). However, some were found in regions free of Fe nanoparticles (Fig. 2c). In contrast, $Fe_{0.5}$-dry contained no large Fe particles and only a few Fe nanoparticles (only 3 out of ~100 particles directly observed had a single small Fe nanoparticle). A characteristic Z-contrast STEM image of $Fe_{0.5}$-dry is shown in Fig. 2d. In the rare case that a Fe nanoparticle was observed, it had a characteristic size of ~1 nm as shown in Fig. 2e. Importantly, $Fe_{0.5}$-dry had a much higher density of single atoms than $Fe_{0.5}$-hydrate, as evidenced by comparing the higher density of bright spots assigned to single Fe atoms in Fig. 2f vs. Fig. 2c. The presence of Fe single atoms was confirmed using image processing software as demonstrated for Fig. 2c and Fig. 2f in Supplementary Fig. 5. Therefore, a significant fraction of Fe was present as large Fe particles in $Fe_{0.5}$-hydrate, while HR-STEM unambiguously shows that Fe was present overwhelmingly as single atoms in $Fe_{0.5}$-dry.

The type and distribution of iron in the two Fe—N—C catalysts were then probed by ^{57}Fe Mössbauer spectroscopy at low temperature. The Mössbauer spectrum of $Fe_{0.5}$-dry was fitted with four components (Fig. 1d and Table 1), including two quadrupole doublets D1 and D2 assigned to FeN_4 sites in different oxidation and spin states, one doublet with low QS assigned to superparamagnetic iron nitride, and one sextet with isomer shift (IS) and hyperfine field values matching those of α-Fe. The spectrum of $Fe_{0.5}$-hydrate was fitted with five components. Two sextets were fit with isomer shift (IS) and hyperfine field values matching those of ferric oxide on the one hand and either Fe_3C or Fe nitride on the other hand. Two components were quadrupole doublets D1 and D2 similar to those observed with $Fe_{0.5}$-dry. The final fit component was a doublet with low QS assigned to superparamagnetic iron nitride (Fig. 1e and Table 1). The latter is likely related to the 1 nm Fe particles identified by STEM in both catalysts. Nanometric iron nitride particles are superparamagnetic, and result in a quadrupole doublet signal with IS and QS values similar to those of the fitted grey doublet, when the spectrum is acquired above the blocking temperature (temperature above which the magnetization of a single nanoparticle flips several times during the measurement) [59—62]. Due to their ultra-small size of ~1 nm, the iron-rich nanoparticles detected by HR-STEM in $Fe_{0.5}$-hydrate may remain superparamagnetic even at the low temperature of 5 K, leading to a quadrupole doublet contribution in the Mössbauer spectra. In contrast, the large Fe particles observed by HR-STEM will be magnetically ordered at 5 K, and therefore are likely related to the

Table 1
Fitted parameters from Mössbauer analyses of the $Fe_{0.5}$-hydrate and $Fe_{0.5}$-dry pristine powder catalysts.

	Component	IS (mm/s)	QS (mm/s)	LW (mm/s)	H (Tesla)	Relative Absorption area (%)
$Fe_{0.5}$-hydrate	D1	0.44	1.30	1.11	–	34
	D2	0.51	2.84	1.76	–	30
	Fe nitride	0.42	0.70	1.11	–	14
	Fe oxide	0.42	–	2.47	44.9	19
	Fe_3C or Fe-nitride	0.44	–	0.70	25.2	3
$Fe_{0.5}$-dry	D1	0.38	1.10	1.06	–	71
	D2	0.57	2.77	1.26	–	21
	Fe nitride	0.27	0.71	0.5	–	5
	α-Fe	0.0	–	0.5	33.0	3

sextet signals assigned to ferric oxide and Fe_3C or Fe-nitride sextets. The absence of peaks related to ferric oxide by XRD but its detection by Mössbauer spectroscopy in $Fe_{0.5}$-hydrate suggests that the Fe (hydr)oxide particles are amorphous, as expected since they likely formed when the sample was exposed to air in ambient conditions. Regarding D1 and D2, recent experimental and theoretical studies on Fe–N–C catalysts prepared similarly as the present ones identify D1 as a Fe(III)–N_4 site in high-spin state with an oxygenated species axially adsorbed, while D2 is a Fe(II)–N_4 site in low or medium spin state [60,63].

The pore structure of the two Fe–N–C catalysts was also investigated. Supplementary Fig. 6 shows the N_2 adsorption and desorption isotherms for both catalysts, their pore size distribution and cumulative surface area. The isotherms have similar shapes characteristic for micro and mesoporous materials, with slightly more volume of N_2 adsorbed at low P/P_0 for $Fe_{0.5}$-hydrate. The PSD analysis with the NLDFT method reveals that this is related to slightly more pores with a width in the range of 10–25 Å in $Fe_{0.5}$-hydrate. The cumulative surface area shows that the microporous surface areas (pores up to 20 Å) are 859 and 944 $m^2\ g^{-1}$ for $Fe_{0.5}$-dry and $Fe_{0.5}$-hydrate, respectively, while their BET areas are 1165 and 1015 $m^2\ g^{-1}$ respectively.

In summary, the in-depth structural characterization of the two Fe–N–C materials revealed profound differences in the Fe speciation, as a result of the different oxidation state, hydration and structure of the Fe acetate salts used to prepare them, while the materials' morphologies were comparable. The key difference is the higher density of FeN_4 sites in $Fe_{0.5}$-dry, and the presence of both large and small Fe particles in $Fe_{0.5}$-hydrate while only small Fe particles in low amount were detected in $Fe_{0.5}$-dry. These differences significantly affect their *ex situ* and *in situ* electrochemical behavior, as will be discussed in the next section. Also, it is clear that the anhydrous iron acetate precursor must be stored in a dry and O_2-free environment if it is going to be used to predominantly create single-atom Fe–N–C catalysts.

3.3. Fe–N–C electrochemical characterization

The activity and selectivity towards ORR were measured first by RRDE in 0.1 M KOH. Cyclic voltametry in N_2 showed similar capacitance for the two Fe–N–C catalysts (Fig. 3a), in line with similar BET areas and pore size distribution for the two catalysts. It is noted that no redox peaks were discernible in the CVs, which has been repeatedly observed for NH_3-pyrolyzed Fe–N–C materials and assigned to the surface FeN_4 sites being highly integrated with delocalized π electrons [64,65]. *In situ* X-ray absorption spectra in 0.1 M KOH on materials prepared similarly as those of the present study showed that the average oxidation state of Fe in FeN_4 sites was decreased following the second pyrolysis performed in NH_3 [65]. This can also be related with increased surface basicity, assigned to higher Lewis basicity from specific N-groups formed during NH_3 pyrolysis than formed during Ar pyrolysis.

The ORR polarization curves measured at 1600 rpm rotation rate and shown in Fig. 3b reveal high ORR activity for both materials with an onset potential near 1 V vs. RHE, and high selectivity for four-electron ORR with diffusion-limited current density close to the theoretical value of *ca* 5.5 mA cm^{-2} expected in such conditions. While high, the kinetic activity for $Fe_{0.5}$-hydrate is lower than that of $Fe_{0.5}$-dry, as revealed by *ca* 10 mV negative shift of its polarization curve in the kinetically-controlled region (*i.e.* at 0–2 mA cm^{-2}). After correction of the polarization curves for O_2 diffusion limitation with Koutecky-Levich law, the obtained Tafel plots identify *ca* 30% lower ORR activity at 0.9 V vs. RHE for $Fe_{0.5}$-hydrate vs. $Fe_{0.5}$-dry (Fig. 3c). The ORR mass activity of $Fe_{0.5}$-dry (9.5 A/g at 0.9 V) is similar to that reported recently for a Fe–N–C material prepared identically by our team (6 A/g at 0.9 V), and that was shown by X-ray absorption and Mössbauer spectroscopies to comprise Fe almost exclusively as Fe–N_4 sites [65]. The lower ORR activity of $Fe_{0.5}$-hydrate vs. $Fe_{0.5}$-dry, despite similar overall Fe contents, can be assigned to the lower site density of FeN_4 sites in the former material, combined with lower ORR activity of Fe particles present in $Fe_{0.5}$-hydrate relative to Fe–N_4 sites. It is of note that the ORR mass activity of *ca* 9 A g^{-1} for $Fe_{0.5}$-dry at 0.9 V vs. RHE is among the highest reported to date in alkaline medium [66–70]. Together, these results suggest that there is no significant synergy between the Fe nanoparticles and the FeN_4 sites, in contrast to recent reports [25–28].

The measured ring current during the RRDE experiment was transformed to show that selectivity of both catlaysts for the four-electron ORR. As observed in Fig. 3d, both catalysts showed good selectivity, with <5% peroxide in the potential range 0.35–0.85 V vs. RHE. These comparable selectivities can be interpreted by the fact that similar active sites are responsible for the main ORR reactivity in both materials, namely Fe–N_4 sites. No significant synergy effect was therefore identified between FeN_4 sites and Fe particles with these two catalysts, regarding the four-electron selectivity.

3.4. In situ Fe–N–C testing in AEMFCs

Fig. 4a presents the initial polarization and power density curves for AEMFCs with $Fe_{0.5}$-hydrate and $Fe_{0.5}$-dry cathodes operating at 80 °C with H_2/O_2 reacting gas feeds. The same high-density polyethylene (HDPE) based AEM with radiation-grafted benzyltrimethylammonium cationic head groups was used in all tests [71]. A comparison plot with a high-loading (0.6 $mg_{Pt}\ cm^{-2}$) Pt/C cathode paired with the same anode, membrane and operating conditions is also provided for comparison. Under these conditions, the AEMFC using the $Fe_{0.5}$-dry cathode exhibited higher performance compared to the cell with the $Fe_{0.5}$-hydrate cathode, with peak power densities reaching 1.8 and 1.2 W cm^{-2}, respectively. However, the peak power density is an amalgam of all of the effects in the cell and not directly indicative of the kinetic performance of the catalysts. A much better kinetic comparison is enabled by discussing the behavior at high potentials where the current density is low. At 0.9 V, the current densities for the two catalysts were very similar, 0.071 for $Fe_{0.5}$-dry *vs.* 0.066 A cm^{-2} for $Fe_{0.5}$-hydrate, at almost the same loading. This is in line with the similar ORR activity measured in RDE for both catalysts – though in terms of absolute ORR activity the mass activity at 0.9 V was *ca* ten times lower in the RDE setup (8–9 A/g) compared to the AEMFC (*ca* 70 A/g), which is due to the differences in temperature from RDE to AEMFC as well as the different environment (in 0.1 M KOH saturated in O_2, vs. gas-phase O_2 with humidified AEI). However, as the current density increased, there was a rapid departure between the behavior of the two materials. At 0.80 V, still often considered in the kinetic regime for PGM-free catalysts in operating fuel cells, the current density with $Fe_{0.5}$-dry and $Fe_{0.5}$-hydrate were 0.575 A cm^{-2} and 0.377 A cm^{-2}, respectively, and at 0.6 V the achieved $Fe_{0.5}$-dry MEA current density was 2.52 A cm^{-2}, approximately twice the current density of the $Fe_{0.5}$-hydrate MEA. As the current density increases, the effect of significantly fewer ORR active sites in $Fe_{0.5}$-hydrate becomes thus more pronounced, as local polarization and mass-transport issues start to dominate its behavior, leading to much lower performance in an operating AEMFC relative to $Fe_{0.5}$-dry MEA. These AEMFC results are also in line with the absence of synergy between FeN_4 sites and Fe particles concluded from the RRDE data.

It should also be noted here that the performance of the MEA using the $Fe_{0.5}$-dry catalyst was very encouraging when compared to the MEA with the high loading Pt/C cathode (Fig. 4a). First, the

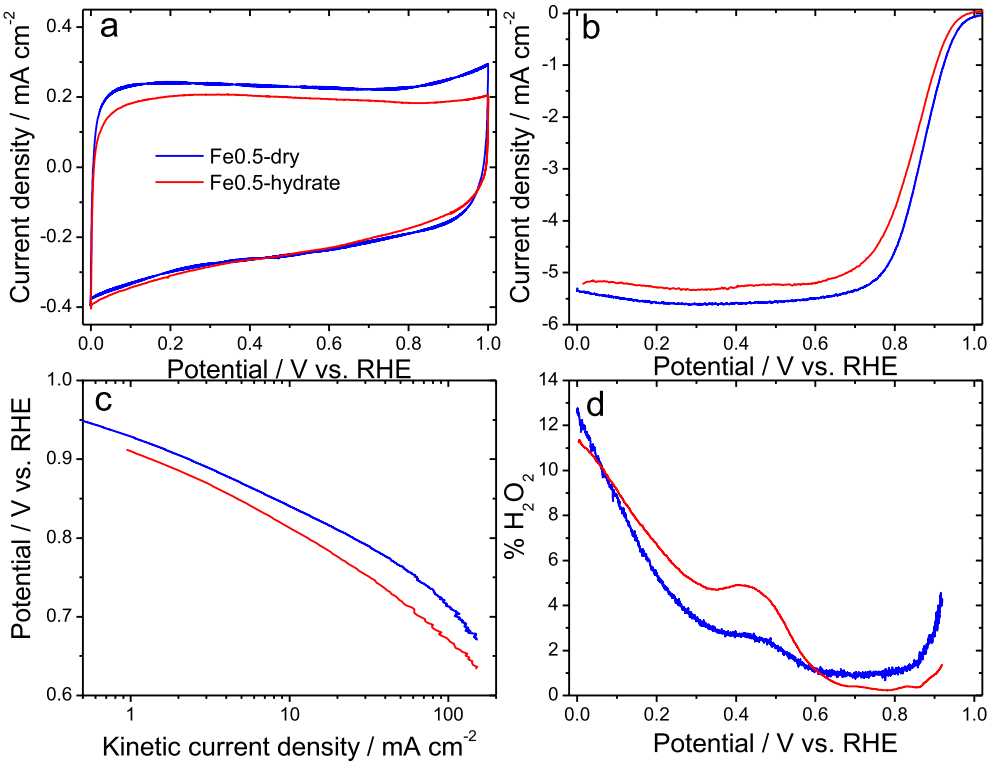


Fig. 3. Electrochemical characterization of $Fe_{0.5}$-hydrate, and $Fe_{0.5}$-dry in RRDE setup. a) Cyclic voltammograms in 0.1 M N_2 saturated KOH electrolyte at a scan rate of 10 mV s^{-1}; b) ORR polarization curves in 0.1 M O_2 saturated KOH electrolyte at a scan rate of 5 mV s^{-1} and rotation rate of 1600 rpm; c) Tafel plots obtained from ORR polarization curves; d) Hydrogen peroxide yield vs. potential. Catalyst loading is 0.2 mg cm^{-2}.

kinetic current density at 0.9 V was superior, 71 mA cm^{-2} vs. 53 mA cm^{-2}. Second, the peak power density of the $Fe_{0.5}$-dry MEA was approximately 70% of the Pt/C MEA. It should also be noted that both the peak power density and mass transport-limited current density are extremely high for a polymer membrane fuel cell using a PGM-free cathode. The performance of the $Fe_{0.5}$-dry MEA is compared to other top AEMFCs with a PGM-free cathode in Supplementary Table 2. MEAs with the $Fe_{0.5}$-dry catalyst also showed very good performance when operating on H_2/air (CO_2-free), achieving a peak power density of 0.7 W cm^{-2} (Fig. 4b).

Next, the stability of the MEA with $Fe_{0.5}$-dry catalyst was investigated in an AEMFC over 105 h at a constant current density of 600 mA cm^{-2} with H_2/air (CO_2-free) reacting gases (Fig. 5a). During this time, the voltage loss was 95 mV. Though this decay rate is somewhat higher than observed on similar AEMFC MEAs with a Pt/C cathode [9], it is promising. To gain more understanding, the voltage loss over time was deconvoluted by looking at the kinetic loss at 0.8 V and the area specific resistance (ASR) value over time. Fig. 5b shows polarization curves acquired at different times during the stability test at 0.6 A cm^{-2}, while Fig. 5c (double y axis) shows both the MEA current density at 0.8 V and the ASR value vs. time. It was observed that the current density at 0.8 V, mostly expected to be controlled by ORR kinetics, decreased by only *ca* 33%, which is far lower than reported for similar Fe–N–C ctalysts after 50–100 h operation in PEMFCs with a similarly prepared Fe–N–C (see e.g. Figs. 2 and 3A in Ref. [72]).

To gain more understanding of the fundamental reasons for the 33% decrease in the ORR activity during the durability test, ^{57}Fe Mössbauer spectroscopy was done on the pristine and end-of-test $^{57}Fe_{0.5}$-dry cathode (Fig. 5d–e). The fitting of the spectra reveals that no new spectral components appeared, and that the absolute amount of Fe–N_4 sites related to the D2 signal were unmodified, while the amount of Fe–N_4 sites related to D1 decreased significantly and the signal for the Fe-oxides (sextet) increased. Overall, the absolute amount of FeN_4 sites (summed on D1+D2) decreased by ca 30% during the test, which agrees well with the relative decrease in the MEA current density at 0.8 V. It suggests that both D1 and D2 are ORR active, but D1 is less stable than D2 in AEMFCs, transforming partially into Fe oxide. These results are in line with a recent work on very similar FeNC catalysts in a PEMFC [73]. The stability of D1 was, however, much better in the AEMFC than in the PEMFC, and the rate of ORR activity loss of the MEA seems to slow down over the 105 h test (Fig. 5c).

Next, it was determined how much of the operating voltage loss could be described directly by the loss of 33% of the FeN_4 catalyst sites. Assuming a Tafel slope of 70 mV/decade for the ORR in AEMFC conditions, such a decrease should only lead to a 12 mV reduction in the cell voltage, which is quite small compared to the total cell voltage decay of 95 mV. Therefore, other factors must be involved in reducing the cell performance. One possibility is the increase in the ASR that was shown in Fig. 5c. Over the 105 h durability experiment, the ASR increased by approximately 10 mΩ cm [2]. Applying Ohm's law, this increase only accounts for a 6 mV reduction in the cell voltage at 0.6 A cm^{-2}. Paired with the 12 mV loss projected from ORR activity decrease, there remains *ca* 77 mV of voltage loss that is unaccounted for after 105 h operation. It is also noteworthy that the mass transport-limited current density at the lowest cell voltage explored (Fig. 5b) is drastically reduced over time. Together, these observations indicate that the main reasons for the decay in cell performance over time is not decreased ORR kinetics nor AEM average conductivity, but likely some mass-transport issues within the Fe–N–C cathode that needed to be further understood.

One possible explanation for the uncompensated 77 mV of performance loss is an exacerbated decrease of OH^- conductivity

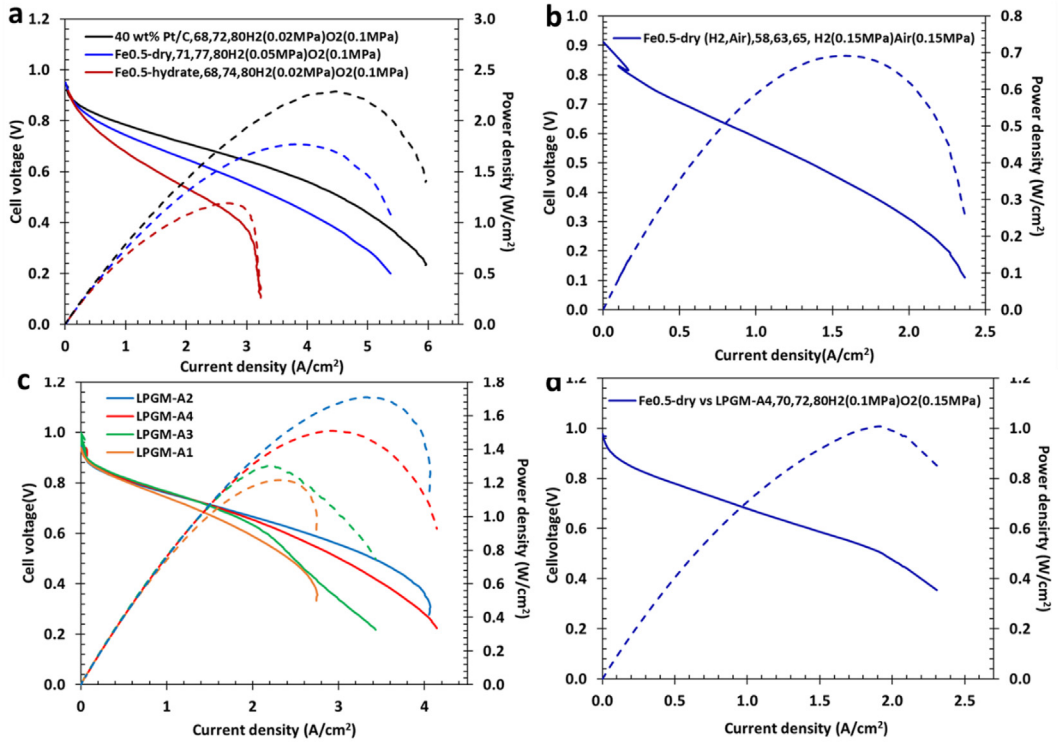


Fig. 4. a-b) AEMFC results with $Fe_{0.5}$-dry and $Fe_{0.5}$-hydrate cathodes. a) H_2/O_2 AEMFC voltage vs. current density (solid) and power density vs. current density (dash) curves for three MEAs. The anode was 0.6 mg cm^{-2} of PtRu and the cathode either 0.91 mg cm^{-2} $Fe_{0.5}$-dry, 1.1 mg cm^{-2} $Fe_{0.5}$-hydrate or 0.5 mg $_{Pt}$ cm^{-2} of Pt/C. The cell was operated at 80 °C under H_2/O_2 flows of 1.0 L min^{-1}. b) H_2/air (CO_2 free) AEMFC voltage vs. current density (solid) and power density vs. current density (dash) curves for an MEA with 0.91 mg cm^{-2} of $Fe_{0.5}$-dry and 0.6 mg PtRu cm^{-2} anode. The cell was operated at 65 °C under H_2/air flows of 1.0 L min^{-1}. c) Current-voltage (solid) and current-power density (dash) curves for AEMFC, which assembled with for H_2–O_2 fuel cells; cathode: 0.5 mg cm^{-2} of Pt/C, different configurations for lowPGM anodes (Supplementary Note 1 and Supplementary Table 1) d) Voltage vs. current density (solid) and power density vs. current density (dash) curves for H_2–O_2 fuel cells with a LPGM-A4 anode, cathode: 0.91 mg cm^{-2} of $Fe_{0.5}$-dry. The membrane used was for all tests was HDPE [71]. (The legends indicate cathode catalyst type, anode and cathode dewpoints, cell temperature, H_2 and O_2 backpressures, in sequence).

through the cathode layer, which is not included in the ASR measurement, rather than a uniform decrease of OH^- conductivity through the AEM only. In the cathode layer, coupled OH^- transport and ORR electrocatalysis can result in severe effects, with or without marginally modifying the AEM overal resistance itself. Exacerbated loss of OH^- conductivity at the cathode is possible in an operating AEMFC due to the dryer environment at the cathode side than at the anode side and poorer chemical stability of the AEI in non-fully humidified conditions [74,75].

To investigate this, a complete MEA numerical model was applied that was previously developed by our team. The model has the ability to calculate the initial steady-state performance of the cell, as well as predict time-changes in ion exchange capacity (IEC) and water content through the MEA, as well as in-cell performance [76–78]. The model is one-dimensional, accounting for mass transport (diffusion of gases and liquid water), ion migration (including osmotic drag of water), and ORR and HOR electrocatalysis (Supplementary Fig. 7). It considers the cathode GDL, cathode CL, AEM, anode CL and anode GDL. The time-dependence is triggered by the degradation of ionomer with time, whose local kinetics is set by the local water content (Supplementary Fig. 8). First, the AEM and ionomer properties were taken from Refs. [53,79]. Then, the main unknown model parameter, specifically the product of ORR exchange current density (i_0) and catalyst specific surface area (A) (the product A x i_0 setting the apparent ORR activity of the cathode), was determined so as to correctly reproduce the initial cell performance (entire polarization curve, and in particular the cell voltage at 0.6 A cm^{-2}) as well as the changes of cell voltage and ASR with time over 105 h of operation. As shown in Supplementary Fig. 8a and b, an excellent agreement was obtained between calculated and experimental data, by tuning only the lump parameter A x i_0. The entire set of model parameters is described in the Supporting Information, with values of other parameters determined based on previous studies and the known design of the experimental MEA. Leaning on the model, profiles of the ion exchange capacity (IEC) as well as hydroxide conductivity across the cell were calculated after 105 h of operation at 0.6 A cm^{-2}. It should be noted that the local conductivity is governed by both local IEC and local water content. Fig. 6a shows a significant decrease in the IEC of the AEM close to the interface with the cathode CL, while the IEC did not decrease through the remainder (*ca* 80%) of the AEM thickness. In the cathode, however, the IEC was reduced by one-half or more throughout the entire CL. This indicates extended degradation of the AEI in the cathode CL, an effect directly resulting from low water content in the cathode CL during operation. Similarly, in Fig. 6b, decreased local OH^- conductivity in the AEM after 105 h operation was observed only close to the cathode CL interface, while the OH^- conductivity was strongly reduced throughout the cathode CL. Quantitatively, the decrease in OH^- conductivity is higher than the decrease in IEC due to the dependency of the hydroxide conductivity on both IEC and water content.

Next, the theoretical analysis of losses through the cell at 0 and 105 h were predicted. Fig. 6c shows that the main difference between the initial and final states of the MEA is the increased gradient of electric potential in the ionomeric phase throughout the cathode CL, resulting in *ca* 100 mV difference throughout the cathode at 105 h compared to the case at 0 h (Fig. 6c). The total

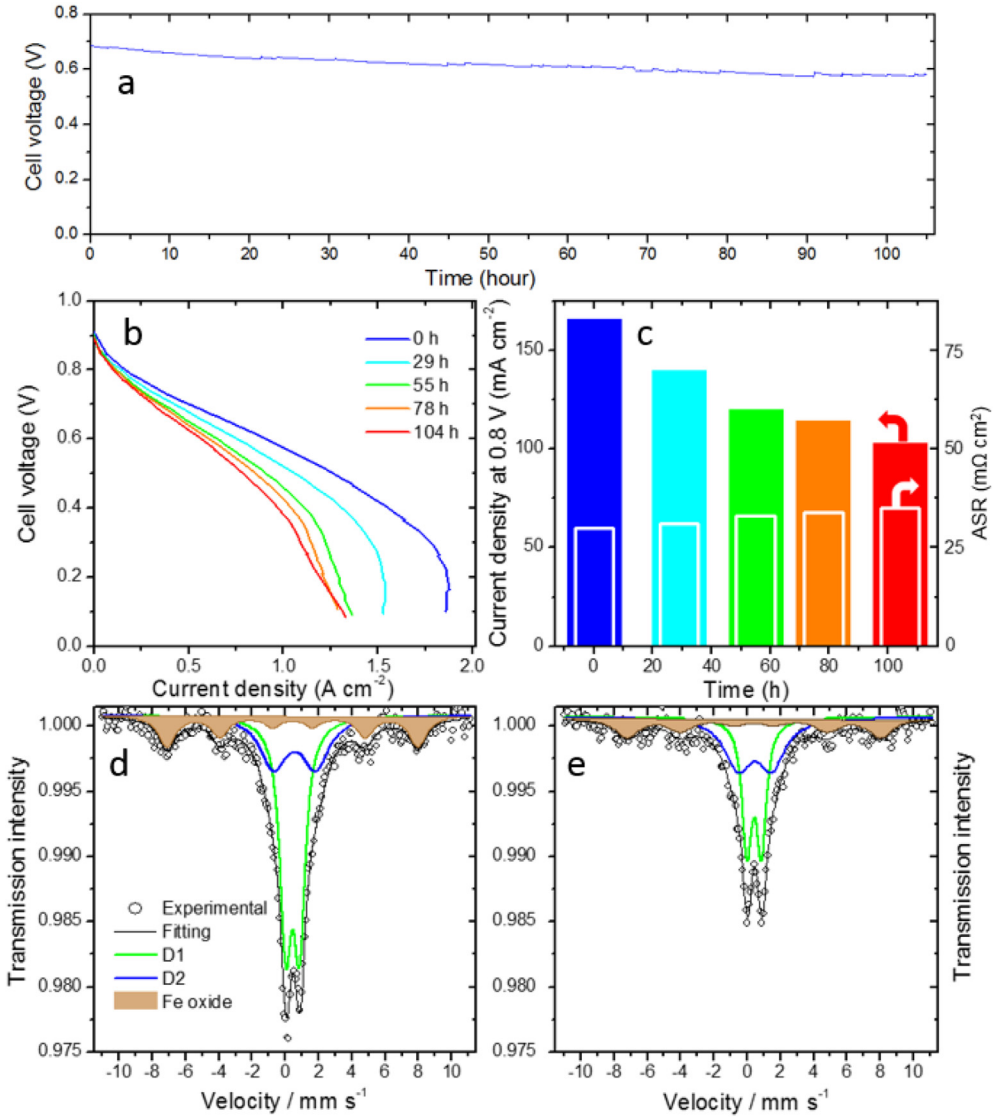


Fig. 5. Durability and insights into the reasons for performance loss during the durability testing with $^{57}Fe_{0.5}$-dry cathode. a) voltage vs. time at a constant current density of 600 mA cm^{-2} under H_2/O_2 flows of 1.0 L min^{-1} with $Fe_{0.5}$-dry cathode. The cell temperature was 65 °C, with the anode and cathode humidification temperature 58 and 62 °C, respectively. The anode and cathode loadings were 0.60 mg_{PtRu} cm^{-2} and 0.91 mg cm^{-2} $Fe_{0.5}$-dry, respectively. The membrane was HDPE. b) the polarization curves and c) the current density at 0.8 V cell voltage and ASR after different durations of galvanostatic hold at 600 mA cm^{-2}). *Ex situ* ^{57}Fe Mössbauer spectra of the $^{57}Fe_{0.5}$-dry cathode d) before and e) after the 105 h galvanostatic hold. The ASR value reported in c) comes from EIS recorded at the current density of 1 A cm^{-2} during the acquisition of the polarization curves. The spectra in d)-e) were fitted with three spectral components (see legend).

anode and cathode overpotentials and iR-drop across the AEM can be extracted from the graph, as represented by the double-sided arrows in Supplementary Fig. 9. From these data, the model predicts that the cathode potential decreased by 100 mV from 0 to 105 h, the iR-drop across the AEM increased by 15 mV, while the anode potential was unmodified. The model also simulated the distribution of the reaction rate throughout each catalyst layer (Fig. 6d). First, the distribution profile of the HOR reaction rate was rather homogeneous initially, and also at the end of test. Only a slightly enhanced reaction rate is observed close to the anode/membrane interface, indicating near full catalyst utilization. On the cathode side, however, the ORR rate was highly inhomogeneous already initially, being higher at the AEM/CL interface than at the CL/GDL interface. This is due to the thicker cathode CL. This effect is exacerbated after 105 h of operation, indicating a further reduced catalyst utilization and, therefore, decreased cathode potential at the current density of 0.6 A/cm^2. This is a direct consequence of the chemical degradation of the ionomeric material within the cathode CL, as shown in Fig. 6a–b by the reduction in the IEC and OH^- conductivity.

Overall, the modeling results identify that the main source for cell performance loss during the galvanostatic hold is due to the cathode, and specifically due to decreased IEC throughout the cathode from chemical degradation due to low water content at the cathode in *operando*. The localized loss of IEC in the AEM near the AEM/cathode CL interface resulted in a mitigated increase in ASR and iR-drop. The decreased OH conductivity through the cathode CL (a domain where both ORR kinetics and OH^- conduction take place) results in decreasing catalyst utilization with the catalytic sites situated far away from the cathode/AEM interface being less and less accessible to hydroxyl ions as the duration of the galvanostatic hold increases. This significant reduction in IEC as well as conductivity of the ionomer through the cathode explains the observed decrease in AEMFC performance during operation.

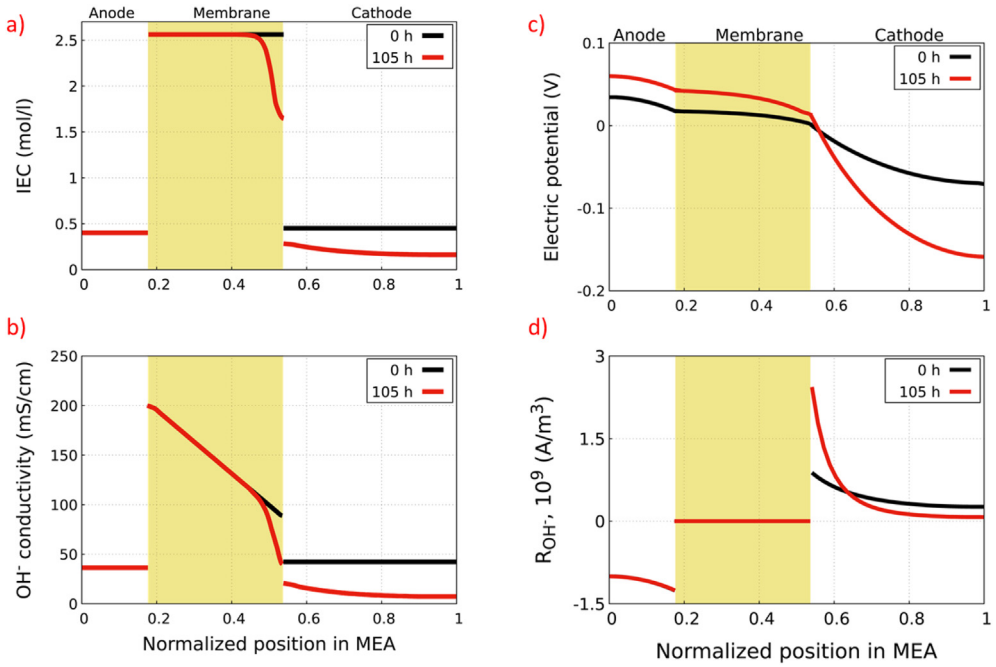


Fig. 6. Calculated profiles of IEC (a), hydroxide conductivity (b), electric potential in the ionomeric phase (c) and reaction rate distribution (d) across the cell at different times (0 and 105 h) after starting AEMFC operation at 0.6 A/cm^2. The origin of the x-axis corresponds to the anode CL −GDL interface.

However, it should be noted that a small decrease in ORR kinetics was observed during the experiment, which was not taken into account in the present model.

3.5. Pairing Fe−N−C cathodes with Low-PGM anodes

While the results shown above with PGM-free cathodes are promising, they were obtained with a high PGM anode, containing itself more PGM than many reported PEMFC MEAs, and higher PGM loading than the DOE targets. One strategy to reach the DOE intermediate targets for AEMFCs, < 0.2 mgPGM cm^{-2}, is to create cells with a PGM-free cathode and low-PGM anode. Therefore, it is essential to investigate anode electrodes that allow for very low catalyst loading while still allowing for the water produced during the HOR to be managed appropriately. Properties such as structure, thickness, porosity, component chemistry, and ionomer:carbon:catalyst ratio all have a significant effect on the water content and balance of the overall cell. Four different low-PGM anode electrodes were designed to investigate the effect of these properties (Supplementary Note 1 and Supplementary Table 1). The performance of these four different electrodes with a Pt/C cathode is shown in Fig. 4c. LPGM-A2 showed the highest peak power density; however, the cell was not properly stable, especially in the mass transport region because of the low thickness of the electrode. The next best design was LPGM-A2, which showed both good performance and also improved stability. This likely indicates that increasing the anode CL thickness has a positive effect on water management.

Next, the cathode with the $Fe_{0.5}$-dry catalyst was paired with the top-performing low-PGM loading anodes, LPGM-A4, and the performance is shown in Fig. 4d. The overall PGM loading for the cell was 0.135 $mg_{PGM}\,cm^{-2}$. Promisingly, this very low PGM-loading AEMFC was able to support a high peak power density of 1.1 W cm^{-2} under H_2/O_2 reacting gases (Fig. 4d). This results in remarkable specific power output, 8.4 $W\,mg_{PGM}^{-1}$ (12.6 $W\,mg_{Pt}^{-1}$)., which is one of the highest of any AEMFC to date (Supplementary Table 2).

4. Conclusions

A highly active PGM-free Fe−N−C catalyst has been reported for the oxygen reduction reaction (ORR) in alkaline media. This catalyst not only shows very high activity *ex situ* but it also was able to achieve high performance in an operating anion exchange membrane fuel cell (AEMFC). A peak power density of 1.8 W cm^{-2} and a mass-transport controlled current density of 6.8 A cm^{-2} on H_2/O_2 reacting gases were achieved. Operating on air, the catalyst was able to support a peak power density of 1.1 W cm^{-2} and achieve stable operation for more than 100 h. During the extended testing, it was shown that only 33% of the catalyst active sites were degraded and an overwhelming portion of the performance loss was due to ionomer degradation from low water content in the cathode – giving direction for future work to further improve PGM-free electrodes.

A key finding of this work is that single-Fe atom sites are crucial to achieve high ORR activity and performance. That was achieved here when the iron precursor was not exposed to water/ambient air, suggesting that the conditions in which some iron precursors are stored (and likely how long it is stored in those conditions) can greatly influence the resulting catalyst structure, activity and performance – verified by XRD, Mössbauer and XANES, RDE and AEMFC testing. In fact, this might explain why many catalysts reported in the literature show quite different intrinsic activity and in-cell performance, despite similar synthesis routes and precursors.

Credit author statement

H.A., P.J.S., F.J. and W.E.M. were the primary writers of the manuscript. H.A. and P.G.S. designed and performed the electrochemical experiments, characterized the catalyst and analyzed the data. H.A. and A.S. together performed the electron microscopy

imaging and further characterization. N.U.H. and X.P. assisted with the AEMFC testing and data analysis. F.J., P.G.S., M.T.S., contributed to synthesizing and providing the material and characterizing the Fe–N–C catalyst. K.Y., I.G.R., S.B., and D.R.D. performed the degradation modeling experiments and analyzed those results. A.Z. performed the Mössbauer spectroscopy and data analysis. J.R.V. oversaw the synthesis of the membrane and ionomer and assisted with the writing of the manuscript. J.R.R. oversaw the electron microscopy experiments and provided ICDD licenses for XRD. W.E.M. supervised the execution of the overall project.

Data availability

The authors declare that all data supporting the findings of this study are available within the paper and Supplementary Information files.

Declaration of competing interest

The authors have no financial or personal conflicts of interest to declare.

Acknowledgements

W.E.M and H.A. gratefully acknowledge the financial support of the U.S. Department of Energy Office of Energy Efficiency & Renewable Energy under the Hydrogen and Fuel Cells Technologies Office (HFTO) (award number: DE-EE0008433) to perform the AEMFC experiments, SEM, TEM, STEM, analyze data and prepare the manuscript. J.R.V. gratefully acknowledges the support of UK EPSRC grant EP/M014371/1 for the polymer synthesis. J.R.R. acknowledges the support of Center of Catalysis for Renewable Fuels(CReF). The work performed by P.G.S and F.J. was supported by the European Union's Horizon 2020 research and innovation programme under grant agreement CREATE [721065]. The portion of the work executed at The Technion was supported by the French-Israeli Joint Research Project (PRC 2019–2021; MOST and CNRS) [PRC2347] (MOST grant No.3-15578); by the Ministry of National Infrastructure, Energy and Water Resources of Israel through grant No. 3-16686 (219-11-135), and the Mauerberger Foundation Fund (MFF). Lastly, we acknowledge Nicolas Donzel, Bernard Fraisse and Nicolas Bibent for N_2 sorption measurements and XRD measurements.

Appendix A. Supplementary data

Supplementary data to this article can be found online at https://doi.org/10.1016/j.mtadv.2021.100179.

References

[1] H.A. Firouzjaie, W.E. Mustain, Catalytic advantages, challenges, and priorities in alkaline membrane fuel cells, ACS Catal. 10 (2020) 225–234.
[2] P.G. Santori, F.D. Speck, S. Cherevko, H.A. Firouzjaie, X. Peng, W.E. Mustain, F. Jaouen, High performance FeNC and Mn-oxide/FeNC layers for AEMFC cathodes, J. Electrochem. Soc. 167 (2020) 134505.
[3] X. Peng, T.J. Omasta, E. Magliocca, L. Wang, J.R. Varcoe, W.E. Mustain, Nitrogen-doped carbon-CoO(x) nanohybrids: a precious metal free cathode that exceeds 1.0Wcm(-2)Peak power and 100 hLife inAnion -ExchangeMembrane fuel cells, Angew Chem. Int. Ed. Engl. 58 (2019) **10**46–1051.
[4] G. Zhang, X. Yang, M. Dubois, M. Herraiz, R. Chenitz, M. Lefèvre, M. Cherif, F. Vidal, V.P. Glibin, S. Sun, J.-P. Dodelet, Non-PGM electrocatalysts for PEM fuel cells: effect of fluorination on the activity and stability of a highly active NC_Ar + NH3 catalyst, Energy Environ. Sci. 12 (2019) 3015–3037.
[5] B.P. Setzler, Z. Zhuang, J.A. Wittkopf, Y. Yan, Activity targets for nanostructured platinum-group-metal-free catalysts in hydroxide exchange membrane fuel cells, Nat. Nanotechnol. 11 (2016) 1020.
[6] S.T. Thompson, D. Peterson, D. Ho, D. Papageorgopoulos, Perspective—the next decade of AEMFCs: near-term targets to accelerate applied R&D, J. Electrochem. Soc. 167 (2020) 84514.
[7] Dr Dimitrios, Papageorgopoulos. Fuel Cell R&D Overview, Fuel Cell Technol. Off., 2019.
[8] G. Huang, M. Mandal, X. Peng, A.C. Yang-Neyerlin, B.S. Pivovar, W.E. Mustain, P.A. Kohl, Composite poly(norbornene) anion conducting membranes for achieving durability, water management and high power (3.4 W/cm2) in hydrogen/oxygen alkaline fuel cells, J. Electrochem. Soc. 166 (2019) F637–F644.
[9] N. Ul Hassan, M. Mandal, G. Huang, H.A. Firouzjaie, P.A. Kohl, W.E. Mustain, Achieving high-performance and 2000 h stability in anion exchange membrane fuel cells by manipulating ionomer properties and electrode optimization, Adv. Energy Mater (2020) 2001986, **n/a**.
[10] J.Y. Cheon, J.H. Kim, J.H. Kim, K.C. Goddeti, J.Y. Park, S.H. Joo, Intrinsic relationship between enhanced oxygen reduction reaction activity and nanoscale work function of doped carbons, J. Am. Chem. Soc. 136 (2014) 8875–8878.
[11] X. Zhang, C. Chen, J. Dong, R.-X. Wang, Q. Wang, Z.-Y. Zhou, S.-G. Sun, Comparative study of the oxygen reduction reaction on pyrolyzed FePc in acidic and alkaline media, ChemElectroChem 5 (2018) 3946–3952.
[12] X. Ge, A. Sumboja, D. Wuu, T. An, B. Li, F.W.T. Goh, T.S.A. Hor, Y. Zong, Z. Liu, Oxygen reduction in alkaline media: from mechanisms to recent advances of catalysts, ACS Catal. 5 (2015) 4643–4667.
[13] R. Nagappan, M. Sanjeev, Fundamental mechanistic understanding of electrocatalysis of oxygen reduction on Pt and non-Pt surfaces: acid versus alkaline media, Adv. Phys. Chem. 2012 (2012) 17.
[14] I. Roche, E. Chaînet, M. Chatenet, J. Vondrák, Carbon-supported manganese oxide nanoparticles as electrocatalysts for the oxygen reduction reaction (ORR) in alkaline medium:physical characterizations and ORR mechanism, J. Phys. Chem. C *11***1** (2007) 1434–1443.
[15] H. Erikson, A. Sarapuu, K. Tammeveski, Oxygen reduction reaction on silver catalysts in alkaline media: a minireview, ChemElectroChem 6 (2019) 73–86.
[16] A. Qaseem, F. Chen, X. Wu, R.L. Johnston, Pt-free silver nanoalloy electrocatalysts for oxygen reduction reaction in alkaline media, Catal. Sci. Technol. 6 (2016) 3317–3340.
[17] J. Lilloja, E. Kibena-Põldsepp, A. Sarapuu, J.C. Douglin, M. Käärik, J. Kozlova, P. Paiste, A. Kikas, J. Aruväli, J. Leis, V. Sammelselg, D.R. Dekel, K. Tammeveski, Transition-metal- and nitrogen-doped carbide-derived carbon/carbon nanotube composites as cathode catalysts for anion-exchange membrane fuel cells, ACS Catal. 11 (2021) 1920–1931.
[18] X. Peng, V. Kashyap, B. Ng, S. Kurungot, L. Wang, R.J. Varcoe, E.W. Mustain, High-performing PGM-free AEMFC cathodes from carbon-supported cobalt ferrite nanoparticles, Catalysts 9 (2019).
[19] Y. Yang, H. Peng, Y. Xiong, Q. Li, J. Lu, L. Xiao, F.J. DiSalvo, L. Zhuang, H.D. Abruña, High-loading composition-tolerant Co–Mn spinel oxides with performance beyond 1 W/cm2 in alkaline polymer electrolyte fuel cells, ACS Energy Lett 4 (2019) 1251–1257.
[20] M.M. Hossen, K. Artyushkova, P. Atanassov, A. Serov, Synthesis and characterization of high performing Fe-N-C catalyst for oxygen reduction reaction (ORR) in Alkaline Exchange Membrane Fuel Cells, J. Power Sources 375 (2018) 214–221.
[21] J. Woo, S.Y. Yang, Y.J. Sa, W.-Y. Choi, M.-H. Lee, H.-W. Lee, T.J. Shin, T.-Y. Kim, S.H. Joo, Promoting oxygen reduction reaction activity of Fe–N/C electrocatalysts by silica-coating-mediated synthesis for anion-exchange membrane fuel cells, Chem. Mater. 30 (2018) 6684–6701.
[22] L. Wang, M. Bellini, H.A. Miller, J.R. Varcoe, A high conductivity ultrathin anion-exchange membrane with 500+ h alkali stability for use in alkaline membrane fuel cells that can achieve 2 W cm−2 at 80 °C, J. Mater. Chem. 6 (2018) 15404–15412.
[23] H.-S. Hu, R.-J. Liu, S. Si, D.-S. Kong, Y.-Y. Feng, Iron and nitrogen codoped carbon catalyst with excellent stability and methanol tolerance for oxygen reduction reaction, Int. J. Energy Res. 43 (2019) 7107–7119.
[24] R. Gokhale, Y. Chen, A. Serov, K. Artyushkova, P. Atanassov, Direct synthesis of platinum group metal-free Fe-N-C catalyst for oxygen reduction reaction in alkaline media, Electrochem. Commun. 72 (2016) 140–143.
[25] X. Ao, W. Zhang, Z. Li, L. Lv, Y. Ruan, H.-H. Wu, W.-H. Chiang, C. Wang, M. Liu, X.C. Zeng, Unraveling the high-activity nature of Fe–N–C electrocatalysts for the oxygen reduction reaction: the extraordinary synergy between Fe–N4 and Fe4N, J. Mater. Chem. 7 (2019) 11792–11801.
[26] X. Ao, W. Zhang, Z. Li, J.-G. Li, L. Soule, X. Huang, W.-H. Chiang, H.M. Chen, C. Wang, M. Liu, X.C. Zeng, Markedly enhanced oxygen reduction activity of single-atom Fe catalysts via integration with Fe nanoclusters, ACS Nano 13 (2019) 11853–11862.
[27] G.-S. Kang, J.-H. Jang, S.-Y. Son, C.-H. Lee, Y.-K. Lee, D.C. Lee, S.J. Yoo, S. Lee, H.-I. Joh, Fe-based non-noble metal catalysts with dual active sites of nanosized metal carbide and single-atomic species for oxygen reduction reaction, J. Mater. Chem. 8 (2020) 22379–22388.
[28] Y. Lei, F. Yang, H. Xie, Y. Lei, X. Liu, Y. Si, H. Wang, Biomass in situ conversion to Fe single atomic sites coupled with Fe2O3 clusters embedded in porous carbons for the oxygen reduction reaction, J. Mater. Chem. 8 (2020) 20629–20636.
[29] M. Primbs, Y. Sun, A. Roy, D. Malko, A. Mehmood, M.-T. Sougrati, P.-Y. Blanchard, G. Granozzi, T. Kosmala, G. Daniel, P. Atanassov, J. Sharman, C. Durante, A. Kucernak, D. Jones, F. Jaouen, P. Strasser, Establishing reactivity descriptors for platinum group metal (PGM)-free Fe–N–C catalysts for PEM fuel cells, Energy Environ. Sci. 13 (2020) 2480–2500.
[30] Y. Shao, J. Dodelet, G. Wu, P. Zelenay, PGM-free cathode catalysts for PEM fuel

cells: a mini-review on stability challenges, Adv. Mater. 31 (2019) 1807615.
[31] E. Proietti, F. Jaouen, M. Lefèvre, N. Larouche, J. Tian, J. Herranz, J.-P. Dodelet, Iron-based cathode catalyst with enhanced power density in polymer electrolyte membrane fuel cells, Nat. Commun. 2 (2011) 416.
[32] K. Kumar, L. Dubau, M. Mermoux, J. Li, A. Zitolo, J. Nelayah, F. Jaouen, F. Maillard, On the influence of oxygen on the degradation of Fe-N-C catalysts, Angew. Chem. Int. Ed. 59 (2020) 3235–3243.
[33] L. Osmieri, D.A. Cullen, H.T. Chung, R.K. Ahluwalia, K.C. Neyerlin, Durability evaluation of a Fe–N–C catalyst in polymer electrolyte fuel cell environment via accelerated stress tests, Nanomater. Energy 78 (2020) 105209.
[34] F. Jaouen, E. Proietti, M. Lefèvre, R. Chenitz, J.-P. Dodelet, G. Wu, H.T. Chung, C.M. Johnston, P. Zelenay, Recent advances in non-precious metal catalysis for oxygen-reduction reaction in polymer electrolyte fuel cells, Energy Environ. Sci. 4 (2011) 114–130.
[35] D. Banham, S. Ye, K. Pei, J. Ozaki, T. Kishimoto, Y. Imashiro, A review of the stability and durability of non-precious metal catalysts for the oxygen reduction reaction in proton exchange membrane fuel cells, J. Power Sources 285 (2015) 334–348.
[36] J. Weiss, H. Zhang, P. Zelenay, Recent progress in the durability of Fe-N-C oxygen reduction electrocatalysts for polymer electrolyte fuel cells, J. Electroanal. Chem. 875 (2020) 114696.
[37] U. Martinez, S. Komini Babu, E.F. Holby, P. Zelenay, Durability challenges and perspective in the development of PGM-free electrocatalysts for the oxygen reduction reaction, Curr. Opin. Electrochem. 9 (2018) 224–232.
[38] S. Wierzbicki, J.C. Douglin, A. Kostuch, D.R. Dekel, K. Kruczała, Are radicals formed during anion-exchange membrane fuel cell operation? J. Phys. Chem. Lett. 11 (2020) 7630–7636.
[39] C.H. Choi, H.-K. Lim, M.W. Chung, G. Chon, N. Ranjbar Sahraie, A. Altin, M.-T. Sougrati, L. Stievano, H.S. Oh, E.S. Park, F. Luo, P. Strasser, G. Dražić, K.J.J. Mayrhofer, H. Kim, F. Jaouen, The Achilles' heel of iron-based catalysts during oxygen reduction in an acidic medium, Energy Environ. Sci. 11 (2018) 3176–3182.
[40] G. Bae, M.W. Chung, S.G. Ji, F. Jaouen, C.H. Choi, pH effect on the H2O2-induced deactivation of Fe-N-C catalysts, ACS Catal. 10 (2020) 8485–8495.
[41] W.E. Mustain, M. Chatenet, M. Page, Y.S. Kim, Durability challenges of anion exchange membrane fuel cells, Energy Environ. Sci. (2020), https://doi.org/10.1039/D0EE01133A.
[42] A. Zadick, L. Dubau, N. Sergent, G. Berthomé, M. Chatenet, Huge instability of Pt/C catalysts in alkaline medium, ACS Catal. 5 (2015) 4819–4824.
[43] Y. Yi, G. Weinberg, M. Prenzel, M. Greiner, S. Heumann, S. Becker, R. Schlögl, Electrochemical corrosion of a glassy carbon electrode, Catal. Today 295 (2017) 32–40.
[44] Y. Lu, L. Wang, K. Preuß, M. Qiao, M.M. Titirici, J. Varcoe, Q. Cai, Halloysite-derived nitrogen doped carbon electrocatalysts for anion exchange membrane fuel cells, J. Power Sources 372 (2017) 82–90.
[45] H. Ren, Y. Wang, Y. Yang, X. Tang, Y. Peng, H. Peng, L. Xiao, J. Lu, H.D. Abruña, L. Zhuang, Fe/N/C nanotubes with atomic Fe sites: a highly active cathode catalyst for alkaline polymer electrolyte fuel cells, ACS Catal. 7 (2017) 6485–6492.
[46] L. Jiao, J. Li, L.L. Richard, Q. Sun, T. Stracensky, E. Liu, M.T. Sougrati, Z. Zhao, F. Yang, S. Zhong, H. Xu, S. Mukerjee, Y. Huang, D.A. Cullen, J.H. Park, M. Ferrandon, D.J. Myers, F. Jaouen, Q. Jia, Chemical vapour deposition of Fe–N–C oxygen reduction catalysts with full utilization of dense Fe–N4 sites, Nat. Mater. (2021), https://doi.org/10.1038/s41563-021-01030-2.
[47] H.A. Gasteiger, S.S. Kocha, B. Sompalli, F.T. Wagner, Activity benchmarks and requirements for Pt, Pt-alloy, and non-Pt oxygen reduction catalysts for PEMFCs, Appl. Catal. B Environ. 56 (2005) 9–35.
[48] C.H. Choi, C. Baldizzone, G. Polymeros, E. Pizzutilo, O. Kasian, A.K. Schuppert, N. Ranjbar Sahraie, M.-T. Sougrati, K.J.J. Mayrhofer, F. Jaouen, Minimizing operando demetallation of Fe-N-C electrocatalysts in acidic medium, ACS Catal. 6 (2016) 3136–3146.
[49] V. Goellner, C. Baldizzone, A. Schuppert, M.T. Sougrati, K. Mayrhofer, F. Jaouen, Degradation of Fe/N/C catalysts upon high polarization in acid medium, Phys. Chem. Chem. Phys. 16 (2014) 18454–18462.
[50] T.J. Omasta, L. Wang, X. Peng, C.A. Lewis, J.R. Varcoe, W.E. Mustain, Importance of balancing membrane and electrode water in anion exchange membrane fuel cells, J. Power Sources 375 (2018) 205–213.
[51] T.J. Omasta, A.M. Park, J.M. LaManna, Y. Zhang, X. Peng, L. Wang, D.L. Jacobson, J.R. Varcoe, D.S. Hussey, B.S. Pivovar, W.E. Mustain, Beyond catalysis and membranes: visualizing and solving the challenge of electrode water accumulation and flooding in AEMFCs, Energy Environ. Sci. 11 (2018) 551–558.
[52] S.D. Poynton, R.C.T. Slade, T.J. Omasta, W.E. Mustain, R. Escudero-Cid, P. Ocón, J.R. Varcoe, Preparation of radiation-grafted powders for use as anion exchange ionomers in alkaline polymer electrolyte fuel cells, J. Mater. Chem. 2 (2014) 5124–5130.
[53] L. Wang, J.J. Brink, Y. Liu, A.M. Herring, J. Ponce-González, D.K. Whelligan, J.R. Varcoe, Non-fluorinated pre-irradiation-grafted (peroxidated) LDPE-based anion-exchange membranes with high performance and stability, Energy Environ. Sci. 10 (2017) 2154–2167.
[54] B. Weber, R. Betz, W. Bauer, S. Schlamp, Crystal structure of iron(II) acetate, Z. Anorg. Allg. Chem. 637 (2011) 102–107.
[55] C. Cheng, W.M. Reiff, Electronic and molecular structure of anhydrous ferrous acetate. A weak antiferromagnet containing six-coordinate iron(II) in nonequivalent environments, Inorg. Chem. 16 (1977) 2097–2103.
[56] Laurikėnas, A. Formation peculiarities of iron (III) acetate: potential precursor for iron metal-organic frameworks (MOFs).
[57] S. Musić, M. Ristić, S. Popović, Mössbauer spectroscopic and X-ray diffraction study of the thermal decomposition of Fe(CH3COO)2 and FeOH(CH3COO)2, J. Radioanal. Nucl. Chem. 121 (1988) 61–71.
[58] B.N. Figgis, G.B. Robertson, Crystal-Molecular structure and magnetic properties of Cr3 (CH3.COO)6 O Cl.5H2O, Nature 205 (1965) 694–695.
[59] K. Strickland, E. Miner, Q. Jia, U. Tylus, N. Ramaswamy, W. Liang, M.-T. Sougrati, F. Jaouen, S. Mukerjee, Highly active oxygen reduction non-platinum group metal electrocatalyst without direct metal–nitrogen coordination, Nat. Commun. 6 (2015) 7343.
[60] J. Li, M.T. Sougrati, A. Zitolo, J.M. Ablett, I.C. Oğuz, T. Mineva, I. Matanovic, P. Atanassov, Y. Huang, I. Zenyuk, A. Di Cicco, K. Kumar, L. Dubau, F. Maillard, G. Dražić, F. Jaouen, Identification of durable and non-durable FeNx sites in Fe–N–C materials for proton exchange membrane fuel cells, Nat. Catal. (2020), https://doi.org/10.1038/s41929-020-00545-2.
[61] S. Kurian, N.S. Gajbhiye, Magnetic and Mössbauer study of ε-Fe y N (2< y< 3) nanoparticles, J. Nanoparticle Res. 12 (2010) 1197–1209.
[62] L. Wang, J. Yin, L. Zhao, C. Tian, P. Yu, J. Wang, H. Fu, Ion-exchanged route synthesis of Fe 2 N–N-doped graphitic nanocarbons composite as advanced oxygen reduction electrocatalyst, Chem. Commun. 49 (2013) 3022–3024.
[63] T. Mineva, I. Matanovic, P. Atanassov, M.-T. Sougrati, L. Stievano, M. Clémancey, A. Kochem, J.-M. Latour, F. Jaouen, Understanding active sites in pyrolyzed Fe–N–C catalysts for fuel cell cathodes by bridging density functional theory calculations and 57Fe mössbauer spectroscopy, ACS Catal. 9 (2019) 9359–9371.
[64] F. Jaouen, J. Herranz, M. Lefèvre, J.-P. Dodelet, U.I. Kramm, I. Herrmann, P. Bogdanoff, J. Maruyama, T. Nagaoka, A. Garsuch, J.R. Dahn, T. Olson, S. Pylypenko, P. Atanassov, E.A. Ustinov, Cross-laboratory experimental study of non-noble-metal electrocatalysts for the oxygen reduction reaction, ACS Appl. Mater. Interfaces 1 (2009) 1623–1639.
[65] P.G. Santori, F.D. Speck, J. Li, A. Zitolo, Q. Jia, S. Mukerjee, S. Cherevko, F. Jaouen, Effect of pyrolysis atmosphere and electrolyte pH on the oxygen reduction activity, stability and spectroscopic signature of FeNx moieties in Fe-N-C catalysts, J. Electrochem. Soc. 166 (2019) F3311–F3320.
[66] L. Osmieri, L. Pezzolato, S. Specchia, Recent trends on the application of PGM-free catalysts at the cathode of anion exchange membrane fuel cells, Curr. Opin. Electrochem. 9 (2018) 240–256.
[67] H. Su, S. Zhou, X. Zhang, H. Sun, H. Zhang, Y. Xiao, K. Yu, Z. Dong, X. Dai, X. Huang, Metal–organic frameworks-derived core–shell Fe3O4/Fe3N@graphite carbon nanocomposites as excellent non-precious metal electrocatalyst for oxygen reduction, Dalton Trans. 47 (2018) 16567–16577.
[68] M. Rauf, Y.-D. Zhao, Y.-C. Wang, Y.-P. Zheng, C. Chen, X.-D. Yang, Z.-Y. Zhou, S.-G. Sun, Insight into the different ORR catalytic activity of Fe/N/C between acidic and alkaline media: protonation of pyridinic nitrogen, Electrochem. Commun. 73 (2016) 71–74.
[69] H.T. Chung, J.H. Won, P. Zelenay, Active and stable carbon nanotube/nanoparticle composite electrocatalyst for oxygen reduction, Nat. Commun. 4 (2013) 1–5.
[70] S. Ratso, A. Zitolo, M. Käärik, M. Merisalu, A. Kikas, V. Kisand, M. Rähn, P. Paiste, J. Leis, V. Sammelselg, S. Holdcroft, F. Jaouen, K. Tammeveski, Non-precious metal cathodes for anion exchange membrane fuel cells from ball-milled iron and nitrogen doped carbide-derived carbons, Renew. Energy 167 (2021) 800–810, https://doi.org/10.1016/j.renene.2020.11.154.
[71] L. Wang, X. Peng, W.E. Mustain, J.R. Varcoe, Radiation-grafted anion-exchange membranes: the switch from low-to high-density polyethylene leads to remarkably enhanced fuel cell performance, Energy Environ. Sci. 12 (2019) 1575–1579.
[72] R. Chenitz, U.I. Kramm, M. Lefèvre, V. Glibin, G. Zhang, S. Sun, J.-P. Dodelet, A specific demetalation of Fe–N4 catalytic sites in the micropores of NC_Ar + NH3 is at the origin of the initial activity loss of the highly active Fe/N/C catalyst used for the reduction of oxygen in PEM fuel cells, Energy Environ. Sci. 11 (2018) 365–382.
[73] A. Zitolo, N. Ranjbar-Sahraie, T. Mineva, J. Li, Q. Jia, S. Stamatin, G.F. Harrington, S.M. Lyth, P. Krtil, S. Mukerjee, E. Fonda, F. Jaouen, Identification of catalytic sites in cobalt-nitrogen-carbon materials for the oxygen reduction reaction, Nat. Commun. 8 (2017) 957.
[74] C.E. Diesendruck, D.R. Dekel, Water − a key parameter in the stability of anion exchange membrane fuel cells, Curr. Opin. Electrochem. 9 (2018) 173–178.
[75] J. Müller, A. Zhegur, U. Krewer, J.R. Varcoe, D.R. Dekel, Practical ex-situ technique to measure the chemical stability of anion-exchange membranes under conditions simulating the fuel cell environment, ACS Mater. Lett. 2 (2020) 168–173.
[76] D.R. Dekel, I.G. Rasin, M. Page, S. Brandon, Steady state and transient simulation of anion exchange membrane fuel cells, J. Power Sources 375 (2018) 191–204.
[77] D.R. Dekel, I.G. Rasin, S. Brandon, Predicting performance stability of anion exchange membrane fuel cells, J. Power Sources 420 (2019) 118–123.
[78] K. Yassin, I.G. Rasin, S. Brandon, D.R. Dekel, Quantifying the critical effect of water diffusivity in anion exchange membranes for fuel cell applications, J. Membr. Sci. 608 (2020) 118206.
[79] A.L. Gonçalves Biancolli, D. Herranz, L. Wang, G. Stehlíková, R. Bance-Soualhi, J. Ponce-González, P. Ocón, E.A. Ticianelli, D.K. Whelligan, J.R. Varcoe, E.I. Santiago, ETFE-based anion-exchange membrane ionomer powders for alkaline membrane fuel cells: a first performance comparison of head-group chemistry, J. Mater. Chem. 6 (2018) 24330–24341.